






Photoionization of negatively charged NV centers in diamond: Theory and *ab initio* calculationsLukas Razinkovas ^{1,*}, Marek Maciaszek ^{1,2}, Friedemann Reinhard ³, Marcus W. Doherty ⁴, and Audrius Alkauskas ^{1,5,†}¹*Center for Physical Sciences and Technology (FTMC), Vilnius LT-10257, Lithuania*²*Faculty of Physics, Warsaw University of Technology, Koszykowa 75, 00-662 Warsaw, Poland*³*Institute of Physics, University of Rostock, 18059 Rostock, Germany*⁴*Laser Physics Centre, Research School of Physics, Australian National University, Australian Capital Territory 2601, Australia*⁵*Department of Physics, Kaunas University of Technology (KTU), Kaunas LT-51368, Lithuania*

(Received 16 April 2021; accepted 8 November 2021; published 6 December 2021)

We present *ab initio* calculations of photoionization thresholds and cross sections of the negatively charged nitrogen-vacancy (NV) center in diamond. We consider photoionization from the ground 3A_2 and the excited 3E states. After the ionization from the 3E level, we show that the NV center transitions into the metastable 4A_2 electronic state of the neutral defect. We reveal how spin polarization of NV^- gives rise to spin polarization of the 4A_2 state, explaining electron spin resonance experiments. We obtain smooth curves of photoionization cross sections as a function of energy by employing dense k -point meshes for the Brillouin-zone integration together with the band unfolding technique to rectify the distortions of the band structure induced by the artificial periodicity of the supercell approach. Our calculations provide a comprehensive picture of photoionization mechanisms of NV^- . They will be useful in interpreting and designing experiments on charge-state dynamics at NV centers. In particular, we offer a consistent explanation of recent results of spin-to-charge conversion of NV centers.

DOI: [10.1103/PhysRevB.104.235301](https://doi.org/10.1103/PhysRevB.104.235301)**I. INTRODUCTION**

Over the past two decades, the nitrogen-vacancy (NV) center in diamond [1] has become a key platform [2] for testing and eventually implementing various quantum technologies. Most technology-ready applications have been in quantum sensing [3], but progress in quantum communication [4] and quantum computing [5,6] has been eminent too. The spin of the negatively charged NV center can be polarized and read out optically [7]. It has been established that optical excitation can lead to the photoionization of NV^- whereby an electron from the NV center is excited to the conduction band, and NV^- is converted to NV^0 [8–10]. In many situations this is a detrimental process for the operation of NV^- , and it has to be avoided by carefully choosing experimental parameters. Photoionization is also disadvantageous for the potential operation of diamond lasers based on NV centers [11] as it competes with stimulated emission.

However, deliberate photoionization of NV^- can also be beneficial. In particular, it has been used to develop the so-called photocurrent detection of magnetic resonance [12–14]. Photoionization of NV centers is also used for spin readout via spin-to-charge conversion [15–17]. Lastly, excitation to the conduction band plays an essential role in a proposed protocol to couple two remote NV centers using spatial stimulated Raman adiabatic passage [18].

The atomic structure of the NV center is shown in Fig. 1(a). The energy-level diagram in Fig. 1(b) depicts the electronic states of NV^- : spin-triplet states 3A_2 and 3E and metastable spin singlets 1E and 1A_1 . It has been established that photoionization of NV^- can occur either via a one-photon or a two-photon mechanism [8–10]. In a single-photon ionization, an electron from the 3A_2 ground state is directly promoted to the conduction band. The threshold for the process has been experimentally determined to be ~ 2.6 eV in Ref. [10] and ~ 2.7 eV in Ref. [19]. The second mechanism is a sequential process of a two-photon absorption [8–10]. In this case, the NV center is first excited to the 3E state; the zero-phonon line (ZPL) of this transition is $E_{ZPL} = 1.945$ eV [1]. Subsequently, the NV center is ionized from the 3E state. In most practical situations, both when photoionization is beneficial or detrimental, the latter process is most important [8–10]. These two processes do not exhaust all the possibilities. After the absorption of the first photon, the NV center can undergo an intersystem crossing (ISC) to the singlet 1A_1 level (Fig. 1) [1]. This is a short-lived state with a lifetime of 0.1 ns [20] from which there is a mostly nonradiative transition to the 1E singlet. The latter is a long-lived state with a lifetime 150–450 ns [21], enabling photoionization from this level via the absorption of the second photon. This is the third photoionization mechanism. Photoionization from the singlets was invoked previously [22], but the mechanism of the process was not investigated in detail in the literature.

Experimental measurements of photoionization cross sections and thresholds for the NV center are not straightforward, in particular regarding the photoionization from the excited state 3E . The first difficulty is related to the fact that light can

*lukas.razinkovas@ftmc.lt

†audrius.alkauskas@ftmc.lt

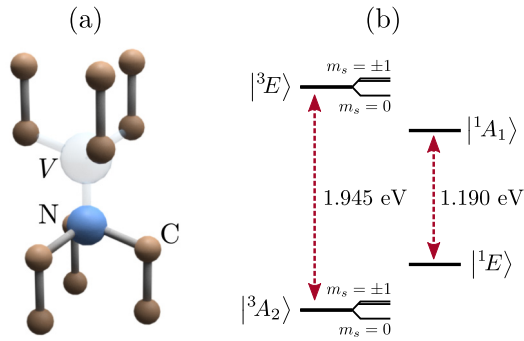


FIG. 1. (a) Atomic structure of the nitrogen-vacancy center in diamond. (b) Electronic level diagram of NV^- . Energies of the ZPL between the triplets and the singlets are indicated. Spin splitting of 3A_2 and 3E states are not to scale.

induce both the transition $NV^- \rightarrow NV^0$ (ionization) and the transition $NV^0 \rightarrow NV^-$ (recombination), often making it hard to disentangle the two processes [8–10]. Moreover, as already mentioned, for the NV center in the excited triplet state, photoionization competes with stimulated emission whereby the NV center returns back to the ground state [11,23], marring the experimental handle of the photoionization process even further. To the best of our knowledge, neither absolute photoionization cross sections from 3A_2 , 3E , and 1E states nor photoionization thresholds from 3E and 1E states have yet been determined experimentally.

In this paper, we address the photoionization thresholds and absolute photoionization cross sections using *ab initio* calculations. In the two-photon ionization, the intradefect absorption precedes the ionization step. Therefore, we calculate the cross section for that process as well. We also report calculations for the cross section of the stimulated emission from the 3E state.

This paper is organized as follows. In Sec. II, we discuss the mechanism of photoionization of NV^- centers in more detail. We give the expressions for photoionization thresholds, cross sections, as well as cross sections for intradefect absorption and stimulated emission. In Sec. III, we discuss the particulars of the electronic structure and introduce computational methods and approximations to calculate cross sections and photoionization thresholds. We present the results of calculations and their analysis in Sec. IV. The consequences of our paper to the physics of NV centers are discussed in Sec. V. Finally, Sec. VI concludes our paper.

The target groups of our paper are: (i) a broad community working on the physics and applications of color centers and (ii) theorists interested in the development of computational methodologies for point defects in solids. The first group can skip a technical Sec. III. In the paper, we use ϵ for photon energies and E for electron energies.

II. NV CENTER PHOTOIONIZATION MECHANISMS

A. Photoionization thresholds

A threshold for photoionization corresponds to an electron being excited to the conduction-band minimum (CBM). In the

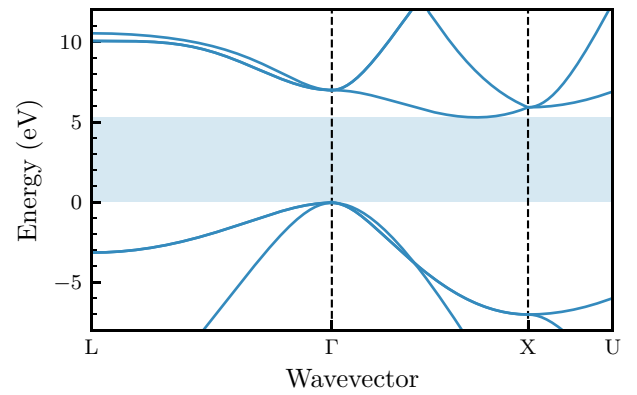


FIG. 2. Band structure of bulk diamond calculated using the HSE density functional (see Sec. III for details about computational methods). The shaded area corresponds to the band gap. The photoionization threshold is determined by electrons being excited to the CBM that occurs between Γ and X points.

case of diamond, the CBM occurs along the Γ - X line in the Brillouin zone as shown in Fig. 2.

1. Photoionization from the 3A_2 state

The ground state of NV^- , 3A_2 , is described by an electron configuration $a_1^2 e^2$ (a_1 and e label irreducible representations of single-particle levels [1]). $m_s = \pm 1$ spin sublevels of the triplet manifold can be described by single Slater determinants. The $m_s = 1$ state is illustrated in Fig. 3(a); in the ket notation it can be written as $|a_1 \bar{a}_1 e_x e_y\rangle$, where “bar” indicates spin-down electrons. Ionization is a process whereby one electron from the e level is excited to the conduction band, turning NV^- into NV^0 [red dotted arrow in Fig. 3(a)]. After NV^- is ionized, it transitions into the 2E ground state of the neutral center with electron configuration $a_1^2 e^1$. The photoionization process can be depicted using the energy-level diagram of the *entire* system, i.e., NV^- or NV^0 plus an electron at the CBM as shown in Fig. 4. The photoionization threshold from the 3A_2 state $IP({}^3A_2)$ has been measured experimentally by Aslam *et al.* [10]. Careful study of charge conversion

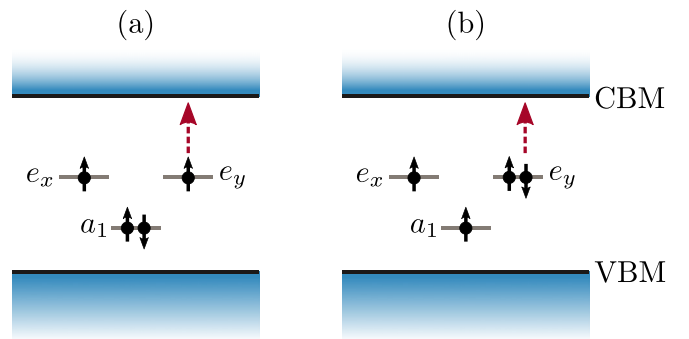


FIG. 3. Photoionization of the NV^- center in the single-electron picture. (a) Electronic configuration of the $m_s = 1$ spin sublevel of the 3A_2 state. (b) Electronic configuration of the $m_s = 1$ spin sublevel of the E_x component of the 3E manifold. Red arrows show one possibility of photoionization whereby an e_y electron is excited to the conduction band (see the text for a more in-depth discussion).

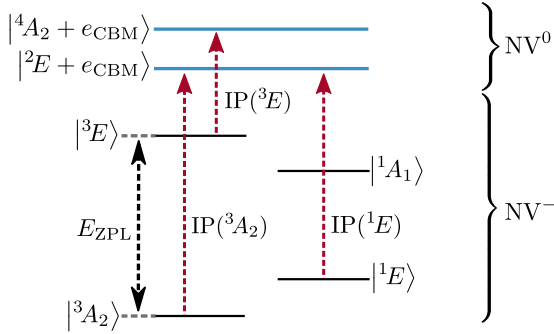


FIG. 4. Photoionization of NV^- from 3A_2 , 3E , and 1E states. Horizontal lines indicate the energy of the entire system: black for NV^- and blue for NV^0 plus an electron at the CBM. Red arrows indicate possible photoionization mechanisms, and E_{ZPL} is the ZPL energy of the triplet transition.

dynamics as a function of wavelength and intensity of laser illumination provided the value $IP({}^3A_2) = 2.6$ eV; the error bar of this value can be assumed to be ~ 0.1 eV [10]. A similar value of 2.7 eV has been obtained in Ref. [19] from the fit of the measured photoionization cross section to an analytical formula. Previous theoretical calculations yielded values $IP({}^3A_2) = 2.64$ eV [24] and 2.74 eV [19], in excellent agreement with both experiments.

2. Photoionization from the 3E state

Compared to the photoionization from the ground state, the physics of the photoionization from the 3E state is presently less understood. The electronic configuration of the 3E state is $a_1^1e^3$. The $m_s = 1$ spin sublevel of the E_x orbital component, $|a_1e_xe_y\bar{e}_y\rangle$, is illustrated in Fig. 3(b). Removing one electron from the e level [red dotted arrow in Fig. 3(b)] yields the configuration $a_1^1e^2$. The lowest-energy state with this configuration is the spin-quartet 4A_2 state of NV^0 . Therefore, the final state of NV^0 after the photoionization is the metastable state 4A_2 and not the ground-state 2E as it was sometimes assumed [9]. The energy-level diagram for this photoionization process is shown in Fig. 4: the initial state is NV^- in the 3E state, whereas the final state is NV^0 in the 4A_2 state plus an electron in the conduction band.

The expression for the threshold of photoionization $IP({}^3E)$ can be read from Fig. 4:

$$IP({}^3E) = IP({}^3A_2) - E_{ZPL} + [E({}^4A_2) - E({}^2E)]. \quad (1)$$

The equation above enables the determination of the threshold for the photoionization from the 3E state. Unfortunately, the energy difference $[E({}^4A_2) - E({}^2E)]$ between the two states of NV^0 is not known experimentally. Therefore, the experimental value of $IP({}^3E)$ cannot be deduced from this relationship. Even though the experimental values of $IP({}^3A_2)$ and E_{ZPL} are known, to benefit from possible cancellation of errors in theoretical calculations, in this paper we will calculate all the quantities that appear in Eq. (1) using the same computational setup, described in Sec. III.

Apart from the 4A_2 state, there are other NV^0 states with the electron configuration $a_1^1e^2$. The second lowest-energy state is 2A_2 [1]. Using the equation similar to Eq. (1), we can

determine the experimental threshold for the photoionization via this process to be about 2.8 eV. This is outside the range of energies we consider in this paper, and this process will be not be analyzed further.

3. Photoionization from the 1E state

Unlike $m_s = \pm 1$ spin sublevels of the triplet states, the two components of the orbital doublet 1E are described by multideterminant wave functions as discussed in, e.g., Ref. [25]. However, as in the case of 3A_2 , the electronic configuration of the 1E state is $a_1^2e^2$. Therefore, after photoionization NV^- center transitions to the 2E ground state of the neutral defect with electronic configuration $a_1^2e^1$. It is straightforward to deduce the photoionization threshold from the 1E state (Fig. 4),

$$IP({}^1E) = IP({}^3A_2) - [E({}^1E) - E({}^3A_2)]. \quad (2)$$

The energy difference $[E({}^1E) - E({}^3A_2)]$ has not yet been measured directly. However, the analysis of the ISC between the 3E and the 1A_1 , as well as the knowledge of the ZPL energy between the two singlets, enables one to determine this energy difference to be about 0.38 eV [26]. As a result, $IP({}^1E)$ can be estimated to be 2.2 ± 0.1 eV.

B. Photoionization cross sections

The general theory of optical absorption in semiconductors is given in a number of textbooks, e.g., Refs. [27,28]. Let $\tilde{\sigma}_{ph}(\epsilon)$ be the photoionization cross section as a function of photon energy ϵ in the absence of lattice relaxation. It is given by (cf. Eq. (10.2.4) in Ref. [28]):

$$\tilde{\sigma}_{ph}(\epsilon) = \frac{4\pi^2\alpha}{3n_D} \epsilon \sum_j r_{ij}^2 \delta(\epsilon - E_{ij}). \quad (3)$$

Here α is the fine-structure constant, and $n_D = 2.4$ is the refractive index of diamond. Label i denotes the initial state Ψ_i , and the sum runs over all final states Ψ_j ; $E_{ij} = E_j - E_i$ is the energy difference between the two states. \vec{r}_{ij} are transition dipole moments (we will also call them optical matrix elements), discussed in Sec. III B. We consider the absorption of light by an ensemble of randomly oriented NV centers. This is the reason for the appearance of the factor $1/3$ in Eq. (3).

Vibrational broadening is introduced by replacing $\delta(\epsilon)$ in Eq. (3) with normalized spectral functions of electron-phonon coupling $A(\epsilon)$, which also includes the contribution of the dynamical Jahn-Teller effect [29] (see Refs. [30,31] for a more thorough discussion). In this case, we can write the actual cross section as a convolution,

$$\sigma_{ph}(\epsilon) = \epsilon \int_{-\infty}^{\infty} \frac{1}{\epsilon'} \tilde{\sigma}_{ph}(\epsilon') A(\epsilon - \epsilon') d\epsilon'. \quad (4)$$

Temperature dependence of the photoionization cross section occurs mainly via the temperature dependence of the spectral functions $A(\epsilon)$. In the remainder of the paper, we will assume a $T = 0$ K limit for these functions.

C. Cross section of the intradefect absorption and stimulated emission

As discussed in Sec. I, photoionization from the 3E state competes with stimulated emission, returning NV^- to the

ground-state 3A_2 . The cross section of stimulated emission (the process ${}^3E \rightarrow {}^3A_2$) is given by an expression:

$$\sigma_{\text{st}}(\epsilon) = \frac{4\pi^2\alpha}{3n_D} \epsilon r_{ij}^2 A(E_{\text{ZPL}} - \epsilon). \quad (5)$$

Here r_{ij} is the optical matrix element for the transition ${}^3A_2 \rightarrow {}^3E$, $E_{\text{ZPL}} = 1.945$ eV, and $A(\epsilon)$ is the spectral function of electron-phonon coupling for stimulated emission, identical to that of spontaneous emission (luminescence).

Another important parameter needed to understand the whole two-step photoionization process is the cross section for intradefect absorption ${}^3A_2 \rightarrow {}^3E$. Its cross section is given by

$$\sigma_{\text{intra}}(\epsilon) = g \frac{4\pi^2\alpha}{3n_D} \epsilon r_{ij}^2 A(\epsilon - E_{\text{ZPL}}). \quad (6)$$

Here $A(\epsilon)$ is a spectral function of electron-phonon coupling for the absorption ${}^3A_2 \rightarrow {}^3E$, and $g = 2$ is the orbital degeneracy factor of the final-state 3E .

III. THEORY AND METHODS

A. Electronic structure methods

Calculations have been performed within the framework of density functional theory (DFT). For the geometry optimization as well as the calculation of excitation energies and ionization thresholds, we used the hybrid exchange-correlation functional of Heyd, Scuseria, and Ernzerhof (HSE) [32]. In this functional, a fraction $a = 1/4$ of screened Fock exchange is admixed to the semilocal exchange based on the generalized gradient approximation in the form of Perdew, Burke, and Ernzerhof (PBE) [33]. As discussed below, to obtain converged photoionization cross sections, we have to perform integration on a dense k -point grid in the Brillouin zone. Unfortunately, such calculations are computationally too expensive if performed with the HSE functional. For this purpose, the optical matrix elements have been calculated using the PBE functional. Our calculations for selected transitions have shown that HSE and PBE matrix elements differ by less than 10%. We used the projector augmented-wave approach with a plane-wave energy cutoff of 500 eV. Calculations have been performed with the Vienna *Ab initio* Simulation Package [34].

The HSE functional provides a very good description of diamond, yielding the band gap of $E_g = 5.34$ eV (experimental value of 5.46 eV) and the lattice constant $a = 3.548$ Å (experimental value of 3.567 Å). Geometry relaxation of the NV center has been performed using $4 \times 4 \times 4$ supercells [35] with 512 atomic sites and a single Γ point for the Brillouin-zone sampling. Ionization potential from ground-state IP(3A_2) has been determined from computed charge-state transition levels as discussed in, e.g., Ref. [35], with finite-size electrostatic corrections of Ref. [36]. Spectral functions of electron-phonon coupling $A(\epsilon)$ that appear in Eq. (4) have been calculated following the methodology of Ref. [31] (see Sec. I of the Supplemental Material [37] for a more detailed discussion). Spectral functions for absorption and stimulated emission in Eqs. (5) and (6) have been taken from Ref. [31].

The energies of excited states 3E and 4A_2 that appear in Eq. (1) have been calculated using the delta-self-consistent-field (Δ SCF) method [38], first applied to the NV center by Gali *et al.* [39]. In order to calculate the energy of the 3E state, the spin-minority electron in the a_1 level is promoted to the e level. The total energy of the 4A_2 state was calculated by setting the spin projection to $m_s = +3/2$. The Δ SCF method typically performs very well when (i) the state is described by a single Slater determinant, and (ii) the state has a different spin and/or orbital symmetry from the ground state [38]. This is indeed the case for 3E and 4A_2 states with spin projections $m_s = \pm 1$ and $m_s = \pm 3/2$, respectively.

B. The nature of electronic states and calculations of optical matrix elements

The initial electronic state Ψ_i that enters in the calculation of the matrix element \tilde{r}_{ij} in Eq. (3) represents the entire solid with an embedded negatively charged defect. The final state Ψ_j represents the solid with a neutral defect plus an excited electron in the conduction band. The optical transition between Ψ_i and Ψ_j must overall be spin conserving.

In this formulation, the optical matrix element \tilde{r}_{ij} and energy difference E_{ij} should be calculated for many-electron states Ψ_i and Ψ_j . The calculation of the matrix elements for multielectron wave functions is a computationally difficult problem, and we will use approximations as described below.

1. Photoionization from the 3A_2 state

Let us first assume that NV^- is initially in the $m_s = 1$ spin sublevel. As already discussed above, this state can be described by a single Slater determinant $|\Psi_i\rangle = |{}^3A_2; 1\rangle = |a_1\bar{a}_1e_xe_y\rangle$ [Fig. 3(a)]. The final state of the entire system that has the same spin is $|\Psi_j\rangle = |({}^2E_{x/y}; \frac{1}{2}) \otimes \phi_c\rangle = |a_1\bar{a}_1e_{x/y}\phi_c\rangle$. It is an antisymmetrized product of NV^0 in the 2E state with the spin projection $m_s = \frac{1}{2}$, $|{}^2E_{x/y}; \frac{1}{2}\rangle = |a_1\bar{a}_1e_{x/y}\rangle$, and a spin-up electron in the conduction band with the wave function ϕ_c . This state has well-defined spin quantum numbers $S = 1$ and $m_s = 1$.

Let $\hat{O} = \sum_i \tilde{r}_i$ be the many-electron dipole operator. To simplify the calculation of matrix elements, we will assume that all single-electron orbitals from which many-electron wave functions are formed are the same in the initial and the final states; the final state differs from the initial one by a single occupied orbital, which corresponds to an electron in the e state being excited to the conduction band. Such simplification allows to adopt the Slater-Condon rule and reduce the matrix element calculated for many-body wave functions to a matrix element between the two Kohn-Sham states,

$$\tilde{r}_{ij} \equiv \langle {}^3A_2; 1 | \hat{O} | ({}^2E_{x/y}; \frac{1}{2}) \otimes \phi_c \rangle = \langle e_{y/x} | \tilde{r} | \phi_c \rangle. \quad (7)$$

As the final state is an orbital doublet, we can calculate, for example, only the transition to the E_x state and multiply the final result by the degeneracy factor $g = 2$. The reasoning for the $m_s = -1$ sublevel is analogous with the only difference being that the spin-down electron is excited to the conduction band.

For $m_s = 0$, the final state is a combination of two spin states of the 2E manifold,

$$|\Psi_j\rangle = \frac{1}{\sqrt{2}} \left[({}^2E_{x/y}; \frac{1}{2}) \otimes \bar{\phi}_c \right] + \frac{1}{\sqrt{2}} \left[({}^2E_{x/y}; -\frac{1}{2}) \otimes \phi_c \right].$$

Here $1/\sqrt{2}$ are Clebsch-Gordan coefficients of spin wave functions, producing the state with $S = 1$ and $m_s = 0$. The squares of Clebsch-Gordan coefficients determine the probability of finding NV^0 in one of the $m_s = \pm 1/2$ substates after photoionization. The resulting optical matrix element is the same as for $m_s = \pm 1$ spin sublevels.

2. Photoionization from the 3E state

For photoionization from the excited state, consider the $m_s = 1$ spin sublevel with the wave function $|\Psi_i\rangle = |{}^3E_{x/y}; 1\rangle = |a_1 e_x e_y \bar{e}_{y/x}\rangle$. The state of the entire system immediately after the ionization is:

$$|\Psi_j\rangle = \frac{\sqrt{3}}{2} \left[({}^4A_2; \frac{3}{2}) \otimes \bar{\phi}_c \right] - \frac{1}{2} \left[({}^4A_2; \frac{1}{2}) \otimes \phi_c \right]. \quad (8)$$

This state has well-defined spin properties (total spin $S = 1$ and spin projection $m_s = 1$). In the equation above, $|({}^4A_2; \frac{3}{2}) \otimes \bar{\phi}_c\rangle = |a_1 e_x e_y \bar{\phi}_c\rangle$ and $|({}^4A_2; \frac{1}{2}) \otimes \phi_c\rangle = 1/\sqrt{3}(|\bar{a}_1 e_x e_y \phi_c\rangle + |a_1 \bar{e}_x e_y \phi_c\rangle + |a_1 e_x \bar{e}_y \phi_c\rangle)$ are antisymmetrized products of wave functions describing NV^0 in the 4A_2 state (with $m_s = 3/2$ or $m_s = 1/2$) and an electron in the conduction band (with $m_s = \pm 1/2$). The matrix element for photoionization can then be shown to be as follows:

$$r_{ij} = \frac{2}{\sqrt{3}} \langle e_{y/x} | \vec{r} | \phi_c \rangle.$$

Equation (8) implies that after the photoionization, the relative probabilities of finding NV^0 in $m_s = 3/2$ and $1/2$ spin sublevels of the 4A_2 state are $3/4$ and $1/4$, respectively. Analogous reasoning as above holds for the photoionization from the $m_s = -1$ spin sublevel of the 3E state with the only difference that the final spin states are $m_s = -3/2$ and $m_s = -1/2$.

For the photoionization from the $m_s = 0$ sublevel, the optical matrix element is the same as for $m_s = \pm 1$ states. In this case, there is an equal probability to find NV^0 in $m_s = \pm 1/2$ spin sublevels of the 4A_2 state.

Relative transition probabilities between spin sublevels of 3E and 4A_2 manifolds are summarized in Fig. 5.

3. Photoionization from the 1E state

The two orbital components of the 1E state can be written as $|{}^1E_x\rangle = 1/\sqrt{2}(|a_1 \bar{a}_1 e_x \bar{e}_x\rangle - |a_1 \bar{a}_1 e_y \bar{e}_y\rangle)$ and $|{}^1E_y\rangle = 1/\sqrt{2}(|a_1 \bar{a}_1 \bar{e}_x e_y\rangle - |a_1 \bar{a}_1 e_x \bar{e}_y\rangle)$ [41]. Immediately after the photoionization the spin-singlet wave function of the entire system is:

$$|\Psi_j\rangle = \frac{1}{\sqrt{2}} \left[({}^2E_{x/y}; \frac{1}{2}) \otimes \bar{\phi}_c \right] - \frac{1}{\sqrt{2}} \left[({}^2E_{x/y}; -\frac{1}{2}) \otimes \phi_c \right].$$

The optical matrix element for this transition can be shown to be the same as for the transition from the 3A_2 state, i.e., $\langle e_{x/y} | \vec{r} | \phi_c \rangle$ and the degeneracy factor $g = 2$.

Due to the multideterminant nature of 1E , applying Δ SCF procedure to calculate its energy is not straightforward. From

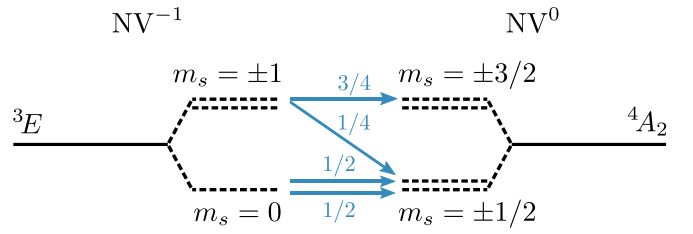


FIG. 5. Spin physics of the photoionization from the 3E state. Numbers near arrows show relative probabilities of the transition during photoionization. The $m_s = +1$ (-1) spin sublevel transitions into either the $m_s = +3/2$ ($-3/2$) or the $m_s = +1/2$ ($-1/2$) sublevel of the 4A_2 manifold with different probabilities. The $m_s = 0$ sublevel transitions to the $m_s = \pm 1/2$ sublevels with equal probabilities. Spin sublevels are separated by zero-field splittings $D({}^3E) = 1.42$ GHz [1] and $D({}^4A_2) = 1.69$ GHz [40].

the theoretical standpoint, there is no consensus regarding the position of this state above the 3A_2 ground state [1]. However, as discussed in Sec. II A 3, the energy difference of $[E({}^1E) - E({}^3A_2)] = 0.38$ eV was obtained in Ref. [26]. The main focus of the current paper is photoionization from the triplet states, so in the case of photoionization from 1E , our calculations will be more approximate. To make calculations possible, we will assume that optical matrix elements are identical to those of the photoionization from the 3A_2 state. In addition, we will use the same spectral function $A(\epsilon)$ as for the ground state, ignoring the occurrence of the Jahn-Teller effect in the 1E state. The resulting cross section is nearly identical to the 3A_2 state with the only difference being that the energies appearing in Eqs. (3) and (4) differ for the two processes.

4. Calculation of optical matrix elements and transition energies

Applying the Slater-Condon rule enables us to evaluate the transition dipole moment \vec{r}_{ij} for Kohn-Sham states ψ_i and ψ_j rather than many-electron states Ψ_i and Ψ_j . Optical matrix elements are calculated as $\vec{r}_{ij} = \langle u_i | i \vec{\nabla}_{\vec{k}} | u_j \rangle$, where u_i and u_j are lattice-periodic parts of wave functions ψ_i and ψ_j . Equation (3) is often alternatively formulated in terms of momentum matrix elements [27], defined as $\vec{p}_{ij} = im(\epsilon/\hbar)\vec{r}_{ij}$.

When replacing the many-electron formulation with the formulation based on Kohn-Sham states, E_{ij} in Eq. (3) is the difference between the Kohn-Sham eigenvalues of the defect state and the perturbed bulk state. Since the smallest value of E_{ij} does not necessarily correspond to photoionization thresholds obtained from total energy calculations [$IP({}^3A_2)$ or $IP({}^3E)$], we apply a rigid shift so that calculated cross sections are consistent with thresholds. As discussed in Sec. III B 3, the calculations for the 1E state are more approximate. In this case, we use Kohn-Sham states of the 3A_2 ground state, but the rigid shift of energies corresponds to the estimated threshold $IP({}^1E)$.

C. The choice of the charge state

When replacing many-electron wave functions Ψ with single-particle ones ψ , an important issue arises regarding the charge state for calculating single-particle energies and single-particle Kohn-Sham states.

On the one hand, since a negatively charged defect is the one that is being ionized, performing calculations for a defect in the $q = -1$ charge state could seem natural. However, whereas the defect wave functions are represented correctly in this charge state, conduction-band wave functions are not. Indeed, final state ψ_j is a conduction-band state perturbed by the *neutral* defect but not a negative one. As a result of long-range Coulomb interactions, these perturbations are much more significant for the negatively charged defect.

On the other hand, supercell calculations of the neutral NV center adequately capture perturbations to the conduction bands. Still, these calculations do not give a totally accurate account of the initial defect state. The question is then: Which of the two calculations is more accurate? We can expect that, in comparison to delocalized bulk states, localized defect states are less affected by the charge on the defect. Following the methodology of Ref. [42], we estimated overlap integrals between defect levels in the case of the neutral and the negatively charged defect. Our result shows that more than 99% of the wave-function character of the localized states is preserved when the charge state changes. We conclude that performing calculations in the neutral charge state is a much more accurate approximation. This approximation will be employed in this paper.

D. Brillouin-zone integration and supercell effects

In the supercell formulation, one obtains an appropriately normalized cross section if one replaces the sum over j in Eq. (3) with the sum over k points of the Brillouin zone of the supercell via $\sum_j \rightarrow 1/N \sum_{n,\vec{k}}$, where N is the number of uniformly distributed k points and n runs over all conduction bands states for a fixed \vec{k} . Matrix elements \vec{r}_{ij} are calculated between the defect state and the perturbed conduction-band state (normalized in the supercell) for the same \vec{k} . In practice, the sum is performed in the irreducible wedge of the Brillouin zone.

To converge the cross-section $\sigma_{\text{ph}}(\epsilon)$ for a given supercell, a very dense k -point mesh is required. Increasing the mesh in self-consistent calculations of supercells becomes computationally very expensive even at the PBE level. Charge density converges much faster as the k -point mesh is increased. Thus, we performed self-consistent calculations using the $6 \times 6 \times 6$ Monkhorst-Pack k -point mesh for the charge density. Photoionization cross sections have been calculated by performing non-self-consistent calculations using much denser $14 \times 14 \times 14$ meshes. This way, one obtains photoionization cross sections of a periodically repeated array of NV centers (albeit correctly normalized per one absorber).

The artificial periodicity of the supercell approach gives rise to two undesirable effects: (i) defect-defect interaction and (ii) spurious perturbation of conduction-band states. Aspect (i) affects defect wave functions. To check the convergence of these wave functions as a function of the supercell size, one can, for example, calculate the optical matrix element \vec{r}_{ij} [Eqs. (5) and (6)] for the transition between a_1 and e levels of the NV center. The comparison of $4 \times 4 \times 4$ and $5 \times 5 \times 5$ supercells shows that matrix elements calculated in these two supercells differ by less than 3%.

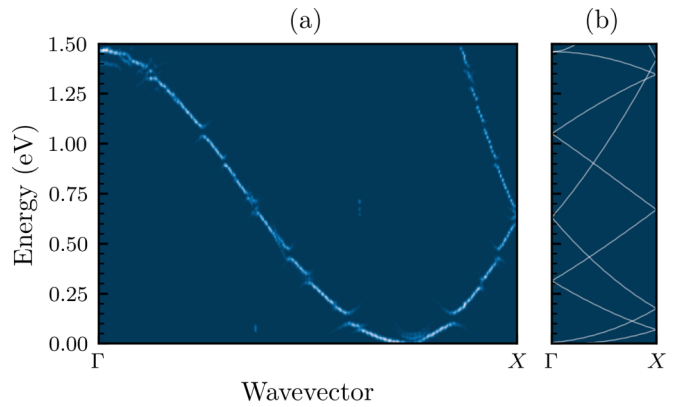


FIG. 6. (a) Unfolded band structure of conduction-band states, perturbed by the NV center, along the Γ - X path. The color indicates a relative spectral weight (dark blue is zero); see Ref. [43] for more details. (b) The band structure of bulk diamond folded to the first Brillouin zone of the $4 \times 4 \times 4$ supercell along the Γ - X path of the supercell.

Effect (ii), however, is more subtle. Periodically repeated NV centers form a superlattice, and one could expect the formation of subbands and the opening of “minigaps” in the same way it occurs in traditional semiconductor superlattices. This is indeed what we observe. In Fig. 6(a), we show the band structure of the $4 \times 4 \times 4$ supercell unfolded [43] onto the Brillouin zone of a primitive diamond cell. For illustration purposes, we choose the band structure of a neutral NV in the 4A_2 state. In Fig. 6(a), one can identify discontinuities in the band structure. To understand why these discontinuities form at specific energies and k vectors, in Fig. 6(b) we show the band structure of bulk diamond *folded* onto the Brillouin zone of the $4 \times 4 \times 4$ supercell. Such folding introduces degeneracies at the band crossing points and Brillouin-zone boundaries. When perturbations, such as the potential of periodically repeated NV centers, are present, these degeneracies are removed, explaining the formation of minigaps in Fig. 6(a). Apart from the density of states (DOS), we find that the values of optical matrix element \vec{r}_{ij} are also affected by artificial periodicity. We observe jumps of r_{ij}^2 across the mini gaps. These jumps can be explained using the textbook picture of the behavior of electronic wave functions close to the band gap in pristine solids via the formation of standing electronic waves (see, e.g., Fig. 3 in Chap. 7 of Ref. [44]). The wave function on one edge of the minigap has a vanishing weight on the NV center, and \vec{r}_{ij} of the transition to this state tends to zero. The wave function on the other edge has maximum weight on the NV center, and \vec{r}_{ij} pertaining to that state attains a finite value. We conclude that artificial periodicity affects both the energies of conduction-band states and the values of optical matrix elements. This is the origin of our observed slow convergence of calculated cross sections as a function of the supercell (not shown), even when the Brillouin-zone integration is already converged.

In this paper, we use the following *ad hoc* solution to this problem. (i) Each perturbed conduction-band state of the defect supercell is unfolded to the Brillouin zone of the primitive cell using the methodology of Ref. [43]. Each k point of the Brillouin zone of the defect supercell unfolds onto several

k points of the Brillouin zone of the primitive cell. (ii) We take the k vector with the highest spectral weight and find the bulk state with the same k , which is closest in energy (typical differences < 0.08 eV). This is the energy that we use in Eq. (3). In this way, we get rid of the discontinuities of the conduction-band state energies. The procedure also yields the band index n . In the case of degeneracy, this k point is assigned to multiple n 's. (iii) For a given perturbed conduction-band state, the value of the optical matrix element r_{ij}^2 is averaged in the Brillouin zone of the primitive cell. The averaging is performed for each n separately, taking the average of the points situated closer than $\Delta r_k = 0.57 \text{ nm}^{-1}$ in the reciprocal space. This smears the jumps of the optical matrix elements across minigaps. The overall procedure results in smooth values of $\sigma_{\text{ph}}(\epsilon)$ as a function of ϵ . The effect of such smoothing is illustrated in Sec. II of the Supplemental Material [37].

E. Local-field effects

In the expressions for photoionization cross-sections (3), (5), and (6), we have omitted so-called local-field effects [27,28]. These effects appear due to the scattering of light on the defect, which can result in the electric field on the defect site being different from that in the bulk. Historically, these effects have been included phenomenologically by multiplying the cross sections by an enhancement factor $(\mathcal{E}_{\text{eff}}/\mathcal{E}_0)^2$; \mathcal{E}_{eff} is the electric field on the defect site, whereas \mathcal{E}_0 is the electric field in the bulk. Classical considerations lead to various models [27,28] from which the so-called Onsager model typically performs best, even though it slightly overestimates the enhancement factor (see Table 10.3 in Ref. [28]). In the Onsager model, the ratio between fields is given by

$$\frac{\mathcal{E}_{\text{eff}}}{\mathcal{E}_0} = \frac{3\epsilon_\infty}{2\epsilon_\infty + 1}, \quad (9)$$

where ϵ_∞ is the dielectric constant of diamond. Using $\epsilon_\infty = 5.7$, we obtain $(\mathcal{E}_{\text{eff}}/\mathcal{E}_0) = 1.38$.

An alternative method to estimate local-field effects is empirical. Radiative emission rate for the ${}^3E \rightarrow {}^3A_2$ transition is given via

$$\Gamma_{\text{rad}} = \frac{1}{\tau_{\text{rad}}} = \left(\frac{\mathcal{E}_{\text{eff}}}{\mathcal{E}_0} \right)^2 \frac{n_D E_{\text{ZPL}}^3 r_{ij}^2}{3\pi \epsilon_0 c^3 \hbar^4}. \quad (10)$$

Here ϵ_0 is vacuum permittivity, and r_{ij} is the transition dipole moment for the transition ${}^3E \rightarrow {}^3A_2$. Comparing the value calculated without local-field effects with the experimental result can provide an estimate for $(\mathcal{E}_{\text{eff}}/\mathcal{E}_0)$. Employing the PBE functional, our calculated radiative lifetime without local field effects is $\tau_{\text{rad}} = 12.2$ ns (using the experimental ZPL energy), in perfect accord with the experimental value $\tau = 12$ ns [1]. This yields $(\mathcal{E}_{\text{eff}}/\mathcal{E}_0) \approx 1.01$. We conclude that the Onsager model overestimates the value of $(\mathcal{E}_{\text{eff}}/\mathcal{E}_0)$, as for F -centers in alkali halides [28]. Note, however, that the theoretical value (and, therefore, possible differences with experiment) are affected not only by the inclusion/exclusion of local fields, but also by other approximations that we employed (density functionals and calculations of matrix elements using Kohn-Sham states). Regardless, we estimate that in the case of NV centers

TABLE I. Thresholds for photoionization from the 3A_2 , 3E , and 1E states of NV^- (in eV). The experimental result for $\text{IP}({}^3A_2)$ is taken from Refs. [10,19]. The value of $\text{IP}({}^1E)$ has not been measured directly but deduced as described in the text (shown in *italic*).

	$\text{IP}({}^3A_2)$	$\text{IP}({}^3E)$	$\text{IP}({}^1E)$
Theory	2.67	1.15	
Experiment	2.6 ^a , 2.7 ^b		2.2

^aReference [10].

^bReference [19].

$(\mathcal{E}_{\text{eff}}/\mathcal{E}_0)$ is in the range of 1–1.4, and very likely close to 1. In the remainder of this paper we will, therefore, set the enhancement factor $(\mathcal{E}_{\text{eff}}/\mathcal{E}_0)^2$ to 1.

IV. RESULTS

A. Excitation energies and photoionization thresholds

We obtain the value $\text{IP}({}^3A_2) = 2.67$ eV for the photoionization threshold from the ground-state 3A_2 , close to previously published *ab initio* results of 2.64 eV [24] and 2.74 [19]. All calculated thresholds are in very good agreement with the experimental values of 2.6 eV [10] and 2.7 eV [19]. This establishes an error bar of about 0.1 eV for the agreement of *ab initio* calculations with experimental data.

The ZPL energy of the intradefect transition ${}^3A_2 \rightarrow {}^3E$ is found to be $E({}^3E) - E({}^3A_2) = 1.996$ eV. This is again in agreement with previous calculations [39] and the experimental value of 1.945 eV, exhibiting an accuracy better than 0.1 eV. Finally, for the energy difference $[E({}^4A_2) - E({}^2E)]$, we obtain the value of 0.48 eV. As discussed in Sec. II A, the experimental energy difference is not available. Previous calculations based on the diagonalization of the Hubbard Hamiltonian (albeit with a rather small basis) [45] yielded a value of 0.68 eV for the vertical transition (i.e., keeping the atoms fixed in the geometry of the 2E) state. Including our calculated relaxation energy of 0.12 eV, we obtain a corrected value of 0.56 eV, in good agreement with our result. Eventually, using Eq. (1), we find the photoionization threshold from the 3E state $\text{IP}({}^3E) = 1.15$ eV. Calculated and experimental thresholds for photoionization from 3A_2 , 3E , and 1E states are summarized in Table I. For the determination of $\text{IP}({}^1E)$, see Sec. II A 3.

B. Cross sections

Before we present the results for NV centers, let us first briefly review some aspects regarding the existing knowledge of photoionization cross sections of deep defects in solids [27]. The overall shape of the function $\tilde{\sigma}_{\text{ph}}(\epsilon)$ depends on the specifics of the defect wave function and of the bulk conduction-band structure. Over the years, many analytical and semi-analytical models of photoionization of deep defects have been developed [27]. Most of these models use the formulation based on the momentum matrix element $\tilde{p}_{ij} = im(\epsilon/\hbar)\tilde{r}_{ij}$, which we will follow in this section.

For the conduction band with a parabolic dispersion close to the CBM, the photoionization threshold corresponds to the excitation to the CBM with the electronic density of states

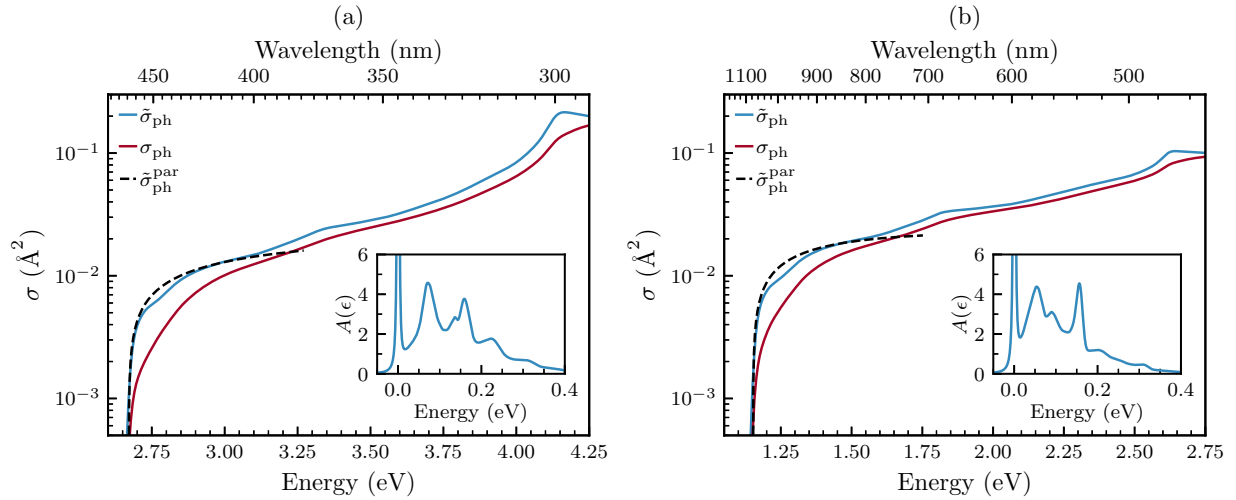


FIG. 7. Photoionization cross sections from (a) the 3A_2 and (b) the 3E state of NV^- . Blue lines: cross sections $\tilde{\sigma}_{ph}(\epsilon)$ with vibrational broadening [Eq. (3)]; red lines: actual cross sections $\sigma_{ph}(\epsilon)$ [Eq. (4)]; dashed lines show $\tilde{\sigma}_{ph}$ calculated using a constant momentum matrix element in Eq. (3) and DOS corresponding to a parabolic band (see text). The insets show the spectral function of electron-phonon coupling $A(\epsilon)$.

$D(E) \sim (E - E_{CBM})^{1/2}$. In this situation, there are two limit cases regarding the dependence of the momentum matrix element \tilde{p}_{ij} on $\Delta\vec{k}$, where $\Delta\vec{k}$ is the quasimomentum measured with respect to the value at the CBM. One limit corresponds to a system where the character of the defect wave function is essentially the same as the character of bulk states near the CBM. In this case, one obtains [27] $\tilde{p}_{ij} \sim \Delta\vec{k}$, which yields the cross section (without electron-phonon coupling) close to the threshold $\tilde{\sigma}_{ph}(\epsilon) \sim (\epsilon - \epsilon_{th})^{3/2}$. Here ϵ_{th} is the threshold for photoionization, e.g., $IP({}^3A_2)$, $IP({}^3E)$, or $IP({}^1E)$ from Table I. One could say that the transition from the defect state to the bulk state at the CBM is dipole-forbidden. The widely used Lucovsky model describes such a scenario [46]. Another limit describes a dipole-allowed transition to the CBM. This happens, for example, when the defect state has p character, whereas the conduction-band states have s character or vice versa. In this case \tilde{p}_{ij} is constant for small $\Delta\vec{k}$ [27], and one obtains $\tilde{\sigma}_{ph}(\epsilon) \sim (\epsilon - \epsilon_{th})^{1/2}$ close to the absorption edge.

The photoionization cross section $\tilde{\sigma}_{ph}(\epsilon)$ for the ground-state 3A_2 is shown in Fig. 7(a) (blue solid line). δ functions in Eq. (3) have been replaced by Gaussians with width $\sigma = 30$ meV. We find that near the threshold $\tilde{\sigma}_{ph}(\epsilon) \sim (\epsilon - \epsilon_{th})^{1/2}$, indicating that the transition to the band edge is dipole allowed and the momentum matrix element near the CBM attains a constant value (see Sec. III of the Supplemental Material [37]). $\tilde{\sigma}_{ph}(\epsilon)$ pertaining to this constant value of the momentum matrix element and DOS corresponding to a parabolic band is also shown in Fig. 7(a) (dashed line). Parabolic dispersion is characterized by effective electron masses m_{\parallel} and m_{\perp} . In our calculations, we used our obtained theoretical values $m_{\parallel} = 1.66m_e$ and $m_{\perp} = 0.32m_e$ that are in good agreement with experimental ones [47]. At larger photon energies, $\tilde{\sigma}_{ph}(\epsilon)$ starts to deviate from the $(\epsilon - \epsilon_{th})^{1/2}$ behavior because the DOS of conduction-band states departs from that of the parabolic band and momentum matrix elements begin to differ from the value at the threshold [37]. For example, visible features at 3.35 eV for the photoionization from the 3A_2

state and at 1.85 eV for the photoionization from the 3E are van Hove singularities reflecting the transition to the conduction-band states at the X point. Lastly and most importantly, Fig. 7(a) shows the actual photoionization cross-section $\sigma_{ph}(\epsilon)$ (dark red line) that includes the effects of vibrational broadening; the inset depicts the spectral function of electron-phonon coupling $A(\hbar\omega)$ [31,37]. Vibrational broadening shifts the weight of the cross section to higher energies, and $\sigma_{ph}(\epsilon)$ no longer exhibits the square-root behavior close to the absorption edge. In passing, we note that the results regarding a constant value of p_{ij} around the CBM confirm the assumptions and the value of the momentum matrix element used in our recent calculations on NV centers in diamond nanowires [18].

Calculated cross sections for the photoionization from the 3E state are shown in Fig. 7(b). The behavior of $\tilde{\sigma}_{ph}(\epsilon)$ as a function of photon energy ϵ (blue line) can be explained similar to the ground state. In short: (i) close to the threshold $\tilde{\sigma}_{ph}(\epsilon) \sim (\epsilon - \epsilon_{th})^{1/2}$ (dashed line); (ii) at larger photon energies $\tilde{\sigma}_{ph}(\epsilon)$ starts to deviate from this functional form because the electronic DOS departs from that of the parabolic band and momentum matrix elements can no longer be assumed constant; (iii) actual photoionization cross-section $\sigma_{ph}(\epsilon)$, which includes the vibrational broadening, exhibits a blueshift with respect to $\tilde{\sigma}_{ph}(\epsilon)$ (dark red line).

The main results of the current paper are presented in Fig. 8. The photoionization cross section from the excited-state 3E (solid blue line) is shown together with the calculated cross sections for stimulation emission $\sigma_{st}(\epsilon)$ from the excited-state 3E [Eq. (5), dark red line], absorption from the ground-state 3A_2 [Eq. (6), orange line], and photoionization cross section from the 1E state (dashed blue line). Photoionization cross section from the 3A_2 state is not shown. The result for $\sigma_{st}(\epsilon)$ is in good agreement with the one presented by Nair *et al.* in Ref. [23]. In that paper, the value of the cross section was deduced from the expression identical to Eq. (5), but using the experimental value of the optical matrix

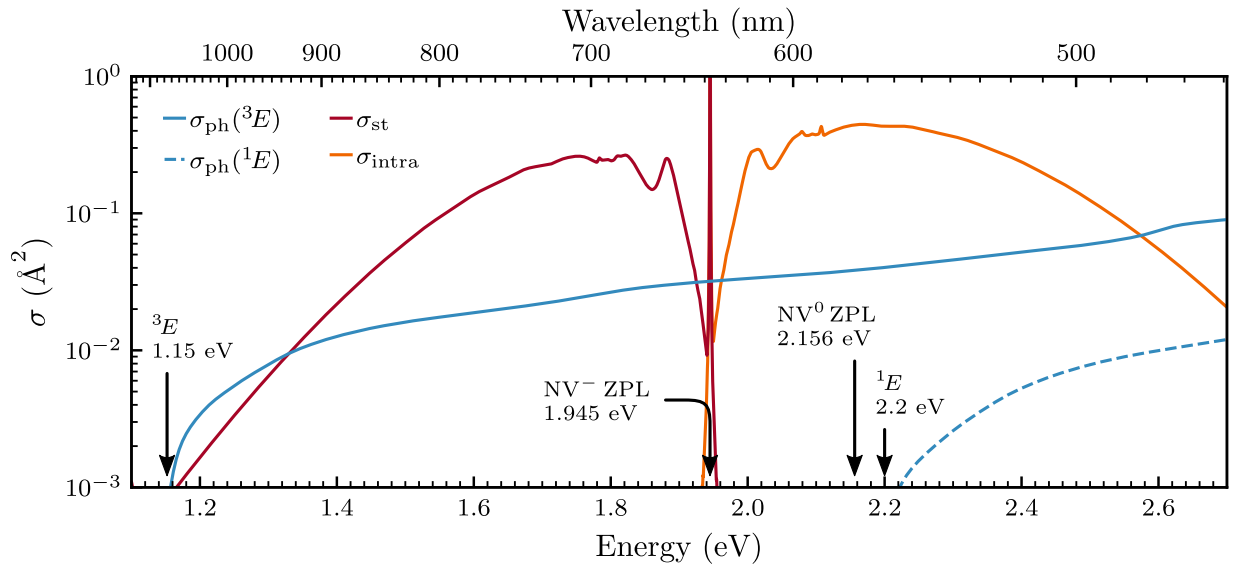


FIG. 8. Calculated cross section as a function of photon energy. Solid blue: photoionization from the excited-state 3E , σ_{ph} ; dark red: stimulated emission, σ_{st} ; orange: intradefect absorption, σ_{intra} ; dashed blue: photoionization from the singlet state 1E . Photoionization thresholds from 3E and 1E are indicated (estimated error bar 0.1 eV), together with the experimental values of the ZPL energy for NV^- and NV^0 .

element and the experimental spectral function $A(\hbar\omega)$. The optical matrix element was calculated from the experimental value of the spontaneous emission rate as in Eq. (10).

V. DISCUSSION

In this Section we discuss the consequences of our findings for the physics and technology of NV centers.

A. Ensembles vs single NV centers

Up to now, we have considered the optical processes in an ensemble of randomly oriented NV centers. The analysis can be extended to single NVs. This is important for the comparison with available experimental data as many experiments are performed on single centers.

Stimulated emission and intradefect absorption correspond to the transition ${}^3A_2 \leftrightarrow {}^3E$; in the single-electron picture this is a $a_1 \leftrightarrow e$ transition. Group theory dictates that $a_1 \leftrightarrow e$ electrical dipole transitions are polarized perpendicularly to the defect axis, hereafter also called z axis. As a result, cross sections for absorption and stimulated emission depend on the orientation of NV centers with respect to the polarization of laser radiation. As an example, consider [111] diamond and an NV center along the (111) direction. It can be shown that for such NV center $\sigma_{\text{st}}(\epsilon)$ and $\sigma_{\text{intra}}(\epsilon)$ are by a factor $3/2$ larger than those given by Eqs. (5) and (6) and presented in Fig. 8.

The situation is a bit more complex in the case of photoionization. The CBM of diamond comprises six valleys along the (100) family of directions in the reciprocal lattice. The presence of the NV center lowers the point-group symmetry from T_d to C_{3v} . Upon restriction to the C_{3v} point group, the six valleys form linear combinations that result in two a_1 single-electron states and a set of two e doublets. As in the case of stimulated emission and intradefect absorption, excitation

of an electron from an e defect level to a conduction-band state of a_1 symmetry is polarized perpendicularly to the z axis. However, excitation to a conduction-band state of e symmetry can be polarized both perpendicularly to the z axis and along the z axis. We conclude that transition dipole moments pertaining to the photoionization from 3E , 3A_2 , and 1E states can have all spatial directions. This is confirmed by our actual calculations. We find that photoionization cross sections for light polarized in the xy plane are about two times larger than for light polarized along the z axis. As an example, let us again consider [111] diamond and a single NV along the (111) direction. In this case, it can be shown that the photoionization cross-section $\sigma_{\text{ph}}(\epsilon)$ is by a factor $\sim 6/5$ larger than the value for ensembles presented in Figs. 7 and 8.

The analysis above shows that different NV centers can behave differently. The specific situation will depend on the exact experimental realization and has to be considered separately. However, our data for ensembles, together with the information provided in this section, can always be used to obtain the relevant information about a specific single NV. A detailed analysis of photoionization of single NV centers will be published elsewhere.

B. Existing understanding of the photoionization of NV centers

DFT calculations of absorption cross sections from the ground-state 3A_2 have been previously reported in Ref. [19]. Our work differs in the following aspects: (i) We present absolute values for $\sigma_{\text{ph}}(\epsilon)$, whereas in Ref. [19] the cross section has been determined in arbitrary units. (ii) The issues regarding the Brillouin-zone integration and supercell size convergence (see Sec. III D) had not been fully dealt with in Ref. [19], which yielded spurious oscillations of the cross section (Fig. 3 in Ref. [19]). (iii) The coupling to phonons was included in our calculations via the spectral function $A(\hbar\omega)$. In contrast, this coupling was omitted in Ref. [19].

The mechanism of the photoionization process from the excited-state 3E has been first analyzed by Siyushev *et al.* [9]. These authors suggested the following two-step process: (i) The electron is first excited to the conduction band, yielding an intermediate electronic state; (ii) an Auger process takes place in this intermediate state whereby an electron from the conduction-band transitions to the a_1 level, whereas an electron from the e level is excited to the conduction band. Let us discuss these two steps separately.

The intermediate state suggested in Ref. [9] is NV^0 in the 4A_2 electronic state plus an electron in the conduction band. This is evident from the electronic configuration shown in the third panel of Fig. 4(a) in Ref. [9]. Thus, the state right after photoionization is the same as the one identified in our paper, even though the nature of the state was not recognized in Ref. [9]. The following question is then: What happens next? Siyushev *et al.* suggested that the Auger process takes place, whereby NV^0 transitions to the ground-state 2E with the calculated rate $\sim 1 \text{ ns}^{-1}$. If we take an electron diffusion constant in diamond $D \approx 50 \text{ cm}^2 \text{ s}^{-1}$ [48], we can estimate that the emitted electron travels a distance of about 2000 nm within the first nanosecond. At variance, calculations of Ref. [9] have been performed assuming that the electron remains a few nanometers within the defect during the capture process. Effectively, calculations assumed exceedingly large effective electron densities $\sim 3 \times 10^{20} \text{ cm}^{-3}$ (one electron per computational supercell). Thus, we conclude: (i) Auger capture rates have been significantly overestimated in these calculations. (ii) Even these overestimated rates indicate that electrons leave the defect site during the computed capture time. Although we do not exclude the Auger process at all, our analysis indicates that this process is highly unlikely. Instead, as we propose in the current paper, the photoexcited electron leaves the defect center, and the NV center remains in the metastable 4A_2 electronic state of NV^0 . Analysis of subsequent processes taking place in the neutral charge state are beyond the scope of this paper.

C. 4A_2 as a state of NV^0 directly after photoionization

The fact that after the photoionization from the 3E state NV centers transition into the metastable 4A_2 state of NV^0 has important consequences for charge dynamics of NV centers. As mentioned above, in Ref. [40] Felton *et al.* observed a strong ESR signal attributed to the 4A_2 state. The existence of the signal implies spin polarization in the 4A_2 manifold that has hitherto been unexplained. Here we propose an explanation for the observed spin polarization.

In Sec. III B 2 we discussed the spin physics of the photoionization from the 3E state. Figure 5 summarizes transitions from different sublevels of the 3E manifold of NV^- to spin sublevels of the 4A_2 manifold of NV^0 . Numbers indicate relative transition probabilities from a given state. In particular, if the defect is initially in the $m_s = +1$ (-1) spin sublevel, the likelihood of the transition to the $m_s = +3/2$ ($-3/2$) sublevel is $3/4$, whereas that to the $m_s = +1/2$ ($-1/2$) sublevel is $1/4$. If the initial spin state is $m_s = 0$, NV^0 can be found in either of the $m_s = \pm 1/2$ spin states of the 4A_2 manifold with equal probability after the ionization. Importantly, if NV^- is initially spin unpolarized (occupation of different spin

sublevels is the same), then there is no spin polarization of the 4A_2 state after photoionization.

In Ref. [40], the electron spin resonance (ESR) signal of the 4A_2 state was only observed for laser wavelengths above the ZPL of NV^0 center 2.156 eV. For such illumination, the NV center is constantly switching between the negative and the neutral state [8,10]. When the NV center is in the negative charge state, intrinsic processes within the electronic states of NV^- lead to a preferential population of the $m_s = 0$ spin sublevel in the 3A_2 and the 3E spin triplets [1]. Thus, photoionization mostly occurs from the $m_s = 0$ sublevel of the 3E state. As per transition probabilities shown in Fig. 5, $m_s = \pm 1/2$ spin sublevels of 4A_2 are preferentially occupied after the photoionization. Zero-field splitting $D({}^4A_2) = 1.69 \text{ GHz}$ [40] separates $m_s = \pm 1/2$ and $m_s = \pm 3/2$ spin sublevels and thus the population of $m_s = \pm 1/2$ sublevels gives rise to a strong ESR signal. We take the experimental results of Ref. [40] as an indirect confirmation of our proposal regarding the involvement of the 4A_2 state in the photoionization from the 3E state. Simply put, the spin polarization of the 4A_2 state of NV^0 found in Ref. [40] directly stems from the spin polarization of NV^- .

D. Photodynamics of NV centers: comparison with selected experiments

Turning now to our calculated cross sections and their relevance to the photophysics of NV centers, we emphasize that the body of experimental work on charge-state dynamics at NV centers is large. To consistently interpret all of that work, the knowledge of photoionization of NV^- is often insufficient, and the understanding of similar processes for NV^0 is needed. This is especially true for steady-state experiments, where, depending on the wavelength of laser(s), the NV center can constantly switch between the two charge states. As the study of NV^0 is beyond the scope of the current paper, we will focus only on a few selected experiments that we are now able to explain using our data. It is important to stress at the outset that the quality of samples in these studies is crucial. We discuss only experiments performed on high-quality bulk samples and will not mention numerous experiments performed on nanodiamonds. The existence of surfaces and possibly various surface defects make the charge-state dynamics of NV centers in nanodiamonds highly complex and not always reproducible.

Our calculations can be most directly compared to the experiments by Hacquebard and Childress [49]. In that work, the authors used green (531-nm) and infrared (766-nm) picosecond laser pulses to monitor charge-state dynamics of single NV centers in [111] diamond. By modeling their experimental data, the authors could extract relative rates of different transitions. In particular, σ_{st}/σ_{ph} was found to be close to 13 for the 766-nm (1.618-eV) excitation. Unfortunately, the orientation of the NV center was not specified in that study. Assuming that the NV center was along the (111) direction and considering the prefactors for NV centers along this direction (Sec. V A), we obtain from Fig. 8 a value $\sigma_{st}/\sigma_{ph} \approx 10$ for $\epsilon = 1.618 \text{ eV}$. We find that the agreement between our calculations and the results of Hacquebard and Childress is rather good.

Another important set of experiments that we can now explain is spin-to-charge conversion upon dual-beam excitation

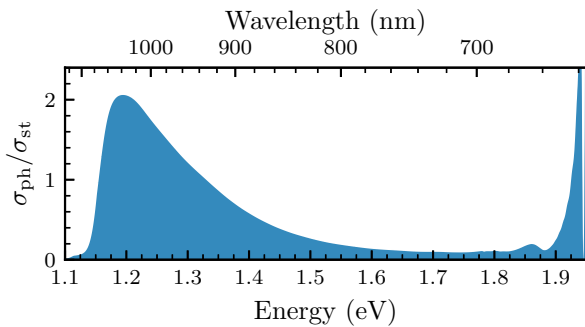


FIG. 9. The ratio of the photoionization cross section and the cross section for stimulated emission $\sigma_{\text{ph}}/\sigma_{\text{st}}$ as a function of photon energy.

at cryogenic temperatures [50,51]. One narrow laser is used in these protocols to resonantly excite NV^- in a preselected spin state, e.g., $m_s = 0$. Another laser pulse is then used to photoionize the defect from the 3E state. In order not to disturb other spin states, the photoionization is performed with sub-ZPL illumination. In the work of Irber *et al.*, efficient photoionization was obtained using a visible laser emitting at 642 nm (1.93 eV) [50]. At variance, Zhang *et al.* used a NIR laser emitting at 1064 nm (1.17 eV) [51]; the overall scheme reached high spin readout fidelities, implying effective photoionization. These results naturally prompt the question: Are these two energies, 1.17 eV and 1.93 eV, special?

We can now answer this question using the results of our calculations. As the angle between single NV centers and the polarization of the ionizing pulse was not known exactly, we use our calculated data for ensembles for semiquantitative analysis. In Fig. 9, we plot the ratio of the photoionization cross section and that for stimulated emission as a function of photon energy. One can identify two regions where photoionization of NV^- with sub-ZPL photons is most efficient ($\sigma_{\text{ph}}/\sigma_{\text{st}} > 1$): (i) just above the threshold energy of 1.15 eV but below ~ 1.3 eV; (ii) just below the ZPL of 1.945 eV. These are exactly the two energy ranges for which the photoionization was successful in the experiments of Refs. [50,51]. We note, however, that the exact value of $\sigma_{\text{ph}}/\sigma_{\text{st}}$ in these two energy windows depends quite sensitively on possible errors

in our calculated value of $\text{IP}({}^3E)$. Despite this, we conclude that our calculations provide a consistent explanation of the results of Refs. [50,51]. Our results point to photon energies where spin-to-charge conversion with sub-ZPL illumination is most efficient.

VI. CONCLUSIONS

This paper presented *ab initio* calculations of photoionization thresholds and cross-sections $\sigma_{\text{ph}}(\epsilon)$ for the negatively charged nitrogen-vacancy center in diamond. From the point of view of computational materials science, our paper introduced a methodology to calculate photoionization cross sections. We employed an integration on a dense k -point mesh together with band unfolding to obtain smooth functions $\sigma_{\text{ph}}(\epsilon)$ over the entire energy range. The methodology is directly applicable to other point defects, including quantum defects [52]. From the point of view of NV physics, we showed that right after the photoionization from the 3E state, the NV^- transitions into the 4A_2 state of NV^0 . This explains spin polarization observed in electron spin resonance experiments of the 4A_2 state. We determine that the photoionization threshold from the 3E state is 1.15 eV. Calculated cross sections helped us interpret recent experiments on spin-to-charge conversion based on dual-beam excitation [50,51]. Our paper provides important knowledge about charge-state dynamics of NV centers that has hitherto been missing.

ACKNOWLEDGMENTS

We acknowledge A. Gali and V. Karpus for useful comments and discussions. This work has been funded by the European Union's Horizon 2020 Research and Innovation Programme under Grant Agreement No. 820394 (Project ASTERIQS). M.M. acknowledges support by the National Science Centre, Poland (Contract No. 2019/03/X/ST3/01751) within the MINIATURA 3 Program. M.W.D. acknowledges support from the Australian Research Council (Grant No. DE170100169). Computational resources were provided by the High Performance Computing center "HPC Saulėtekis" in the Faculty of Physics, Vilnius University and the Interdisciplinary Center for Mathematical and Computational Modelling (ICM), University of Warsaw (Grant No. GB81-6).

-
- [1] M. W. Doherty, N. B. Manson, P. Delaney, F. Jelezko, J. Wrachtrup, and L. C. Hollenberg, The nitrogen-vacancy colour centre in diamond, *Phys. Rep.* **528**, 1 (2013).
- [2] D. D. Awschalom, R. Hanson, J. Wrachtrup, and B. B. Zhou, Quantum technologies with optically interfaced solid-state spins, *Nat. Photonics* **12**, 516 (2018).
- [3] R. Schirhagl, K. Chang, M. Loretz, and C. L. Degen, Nitrogen-vacancy centers in diamond: Nanoscale sensors for physics and biology, *Annu. Rev. Phys. Chem.* **65**, 83 (2014).
- [4] B. Hensen, H. Bernien, A. E. Dréau, A. Reiserer, N. Kalb, M. S. Blok, J. Ruitenberg, R. F. L. Vermeulen, R. N. Schouten, C. Abellán, W. Amaya, V. Pruneri, M. W. Mitchell, M. Markham, D. J. Twitchen, D. Elkouss, S. Wehner, T. H. Taminiau, and R. Hanson, Loophole-free Bell inequality violation using electron spins separated by 1.3 kilometres, *Nature (London)* **526**, 682 (2015).
- [5] C. E. Bradley, J. Randall, M. H. Abobeih, R. C. Berrevoets, M. J. Degen, M. A. Bakker, M. Markham, D. J. Twitchen, and T. H. Taminiau, A Ten-Qubit Solid-State Spin Register with Quantum Memory up to One Minute, *Phys. Rev. X* **9**, 031045 (2019).
- [6] S. Pezzagna and J. Meijer, Quantum computer based on color centers in diamond, *Appl. Phys. Rev.* **8**, 011308 (2021).
- [7] F. Jelezko, T. Gaebel, I. Popa, A. Gruber, and J. Wrachtrup, Observation of Coherent Oscillations in a Single Electron Spin, *Phys. Rev. Lett.* **92**, 076401 (2004).

- [8] K. Beha, A. Batalov, N. B. Manson, R. Bratschitsch, and A. Leitner, Optimum Photoluminescence Excitation and Recharging Cycle of Single Nitrogen-Vacancy Centers in Ultrapure Diamond, *Phys. Rev. Lett.* **109**, 097404 (2012).
- [9] P. Siyushev, H. Pinto, M. Vörös, A. Gali, F. Jelezko, and J. Wrachtrup, Optically Controlled Switching of the Charge State of a Single Nitrogen-Vacancy Center in Diamond at Cryogenic Temperatures, *Phys. Rev. Lett.* **110**, 167402 (2013).
- [10] N. Aslam, G. Waldherr, P. Neumann, F. Jelezko, and J. Wrachtrup, Photo-induced ionization dynamics of the nitrogen vacancy defect in diamond investigated by single-shot charge state detection, *New J. Phys.* **15**, 013064 (2013).
- [11] J. Jeske, D. W. M. Lau, X. Vidal, L. P. McGuinness, P. Reineck, B. C. Johnson, M. W. Doherty, J. C. McCallum, S. Onoda, F. Jelezko, T. Ohshima, T. Volz, J. H. Cole, B. C. Gibson, and A. D. Greentree, Stimulated emission from nitrogen-vacancy centres in diamond, *Nat. Commun.* **8**, 14000 (2017).
- [12] E. Bourgeois, A. Jarmola, P. Siyushev, M. Gulka, J. Hruby, F. Jelezko, D. Budker, and M. Nesladek, Photoelectric detection of electron spin resonance of nitrogen-vacancy centres in diamond, *Nat. Commun.* **6**, 8577 (2015).
- [13] P. Siyushev, M. Nesladek, E. Bourgeois, M. Gulka, J. Hruby, T. Yamamoto, M. Trupke, T. Teraji, J. Isoya, and F. Jelezko, Photoelectrical imaging and coherent spin-state readout of single nitrogen-vacancy centers in diamond, *Science* **363**, 728 (2019).
- [14] M. Gulka, D. Wirtitsch, V. Ivády, J. Vodnik, J. Hruby, G. Magchiels, E. Bourgeois, A. Gali, M. Trupke, and M. Nesladek, Room-temperature control and electrical readout of individual nitrogen-vacancy nuclear spins, *Nat. Commun.* **12**, 4421 (2021).
- [15] G. Waldherr, J. Beck, M. Steiner, P. Neumann, A. Gali, T. Frauenheim, F. Jelezko, and J. Wrachtrup, Dark States of Single Nitrogen-Vacancy Centers in Diamond Unraveled by Single Shot NMR, *Phys. Rev. Lett.* **106**, 157601 (2011).
- [16] B. J. Shields, Q. P. Unterreithmeier, N. P. de Leon, H. Park, and M. D. Lukin, Efficient Readout of a Single Spin State in Diamond Via Spin-To-Charge Conversion, *Phys. Rev. Lett.* **114**, 136402 (2015).
- [17] D. A. Hopper, H. J. Shulevitz, and L. C. Bassett, Spin readout techniques of the nitrogen-vacancy center in diamond, *Micromachines* **9**, 437 (2018).
- [18] L. M. Oberg, E. Huang, P. M. Reddy, A. Alkauskas, A. D. Greentree, J. H. Cole, N. B. Manson, C. A. Meriles, and M. W. Doherty, Spin coherent quantum transport of electrons between defects in diamond, *Nanophotonics* **8**, 1975 (2019).
- [19] E. Bourgeois, E. Londero, K. Buczak, J. Hruby, M. Gulka, Y. Balasubramanian, G. Wachter, J. Stursa, K. Dobes, F. Aumayr, M. Trupke, A. Gali, and M. Nesladek, Enhanced photoelectric detection of NV magnetic resonances in diamond under dual-beam excitation, *Phys. Rev. B* **95**, 041402(R) (2017).
- [20] R. Ulbricht and Z.-H. Loh, Excited-state lifetime of the NV⁻ infrared transition in diamond, *Phys. Rev. B* **98**, 094309 (2018).
- [21] V. M. Acosta, A. Jarmola, E. Bauch, and D. Budker, Optical properties of the nitrogen-vacancy singlet levels in diamond, *Phys. Rev. B* **82**, 201202(R) (2010).
- [22] D. A. Hopper, R. R. Grote, A. L. Exarhos, and L. C. Bassett, Near-infrared-assisted charge control and spin readout of the nitrogen-vacancy center in diamond, *Phys. Rev. B* **94**, 241201(R) (2016).
- [23] S. R. Nair, L. J. Rogers, X. Vidal, R. P. Roberts, H. Abe, T. Ohshima, T. Yatsui, A. D. Greentree, J. Jeske, and T. Volz, Amplification by stimulated emission of nitrogen-vacancy centres in a diamond-loaded fibre cavity, *Nanophotonics* **9**, 4505 (2020).
- [24] P. Deák, B. Aradi, M. Kaviani, T. Frauenheim, and A. Gali, Formation of NV centers in diamond: A theoretical study based on calculated transitions and migration of nitrogen and vacancy related defects, *Phys. Rev. B* **89**, 075203 (2014).
- [25] A. Gali, M. Fyta, and E. Kaxiras, Ab initio supercell calculations on nitrogen-vacancy center in diamond: Electronic structure and hyperfine tensors, *Phys. Rev. B* **77**, 155206 (2008).
- [26] M. L. Goldman, M. W. Doherty, A. Sipahigil, N. Y. Yao, S. D. Bennett, N. B. Manson, A. Kubanek, and M. D. Lukin, State-selective intersystem crossing in nitrogen-vacancy centers, *Phys. Rev. B* **91**, 165201 (2015).
- [27] B. K. Ridley, *Quantum Processes in Semiconductors* (Oxford University Press, Oxford, 2013).
- [28] A. M. Stoneham, *Theory of Defects in Solids* (Oxford University Press, Oxford, 2001).
- [29] G. Davies, The Jahn-Teller effect and vibronic coupling at deep levels in diamond, *Rep. Prog. Phys.* **44**, 787 (1981).
- [30] A. Alkauskas, B. B. Buckley, D. D. Awschalom, and C. G. Van de Walle, First-principles theory of the luminescence lineshape for the triplet transition in diamond NV centres, *New J. Phys.* **16**, 073026 (2014).
- [31] L. Razinkovas, M. W. Doherty, N. B. Manson, C. G. Van de Walle, and A. Alkauskas, Vibrational and vibronic structure of isolated point defects: The nitrogen-vacancy center in diamond, *Phys. Rev. B* **104**, 045303 (2021).
- [32] J. Heyd, G. E. Scuseria, and M. Ernzerhof, Hybrid functionals based on a screened coulomb potential, *J. Chem. Phys.* **118**, 8207 (2003).
- [33] J. P. Perdew, K. Burke, and M. Ernzerhof, Generalized Gradient Approximation Made Simple, *Phys. Rev. Lett.* **77**, 3865 (1996).
- [34] G. Kresse and J. Furthmüller, Efficient iterative schemes for ab initio total-energy calculations using a plane-wave basis set, *Phys. Rev. B* **54**, 11169 (1996).
- [35] C. Freysoldt, B. Grabowski, T. Hickel, J. Neugebauer, G. Kresse, A. Janotti, and C. G. Van de Walle, First-principles calculations for point defects in solids, *Rev. Mod. Phys.* **86**, 253 (2014).
- [36] C. Freysoldt, J. Neugebauer, and C. G. Van de Walle, Fully ab initio Finite-Size Corrections for Charged-Defect Supercell Calculations, *Phys. Rev. Lett.* **102**, 016402 (2009).
- [37] See Supplemental Material at <http://link.aps.org/supplemental/10.1103/PhysRevB.104.235301> for: (i) calculation of spectral densities of electron-phonon coupling and spectral functions $A(\epsilon)$; (ii) illustration of our procedure for the Brillouin-zone integration; (iii) discussion about the energy dependence of optical matrix elements.
- [38] R. O. Jones and O. Gunnarsson, The density functional formalism, its applications and prospects, *Rev. Mod. Phys.* **61**, 689 (1989).
- [39] A. Gali, E. Janzén, P. Deák, G. Kresse, and E. Kaxiras, Theory of Spin-Conserving Excitation of the N-V Center in Diamond, *Phys. Rev. Lett.* **103**, 186404 (2009).

- [40] S. Felton, A. M. Edmonds, M. E. Newton, P. M. Martineau, D. Fisher, and D. J. Twitchen, Electron paramagnetic resonance studies of the neutral nitrogen vacancy in diamond, *Phys. Rev. B* **77**, 081201(R) (2008).
- [41] M. W. Doherty, N. B. Manson, P. Delaney, and L. C. L. Hollenberg, The negatively charged nitrogen-vacancy centre in diamond: the electronic solution, *New J. Phys.* **13**, 025019 (2011).
- [42] M. E. Turiansky, A. Alkauskas, M. Engel, G. Kresse, D. Wickramaratne, J.-X. Shen, C. E. Dreyer, and C. G. Van de Walle, Nonrad: Computing nonradiative capture coefficients from first principles, *Comput. Phys. Commun.* **267**, 108056 (2021).
- [43] V. Popescu and A. Zunger, Extracting e versus k effective band structure from supercell calculations on alloys and impurities, *Phys. Rev. B* **85**, 085201 (2012).
- [44] C. Kittel, *Introduction to Solid State Physics* (Wiley, Hoboken, NJ, 2004).
- [45] A. Ranjbar, M. Babamoradi, M. Heidari Saani, M. A. Vesaghi, K. Esfarjani, and Y. Kawazoe, Many-electron states of nitrogen-vacancy centers in diamond and spin density calculations, *Phys. Rev. B* **84**, 165212 (2011).
- [46] G. Lucovsky, On the photoionization of deep impurity centers in semiconductors, *Solid State Commun.* **3**, 299 (1965).
- [47] F. Nava, C. Canali, C. Jacoboni, L. Reggiani, and S. Kozlov, Electron effective masses and lattice scattering in natural diamond, *Solid State Commun.* **33**, 475 (1980).
- [48] M. Nesladek, A. Bogdan, W. Deferme, N. Tranchant, and P. Bergonzo, Charge transport in high mobility single crystal diamond, *Diam. Relat. Mater.* **17**, 1235 (2008).
- [49] L. Hacquebard and L. Childress, Charge-state dynamics during excitation and depletion of the nitrogen-vacancy center in diamond, *Phys. Rev. A* **97**, 063408 (2018).
- [50] D. M. Irber, F. Poggiali, F. Kong, M. Kieschnick, T. Lühmann, D. Kwiatkowski, J. Meijer, J. Du, F. Shi, and F. Reinhard, Robust all-optical single-shot readout of nitrogen-vacancy centers in diamond, *Nat. Commun.* **12**, 532 (2021).
- [51] Q. Zhang, Y. Guo, W. Ji, M. Wang, F. Yin, Junand Kong, Y. Lin, C. Yin, F. Shi, Y. Wang, and J. Du, High-fidelity single-shot readout of single electron spin in diamond with spin-to-charge conversion, *Nat. Commun.* **12**, 1529 (2021).
- [52] L. Bassett, A. Alkauskas, A. Exarhos, and K.-M. Fu, Quantum defects by design, *Nanophotonics* **8**, 1867 (2019).